International Journal of Mathematical, Engineering and Management Sciences
Vol. 9, No. 1, 1-22, 2024
https://doi.org/10.33889/IJMEMS.2024.9.1.001

Ram Arti Publishers

Insight on the Flow Physics of Shock-driven Elliptical Gas Inhomogeneity with Different Atwood Numbers

Satyvir Singh
Applied and Computational Mathematics,
RWTH Aachen University, Aachen, Germany.
Corresponding author: singh@acom.rwth-aachen.de

Bidesh Sengupta
School of Computer Science and Engineering,
Nanyang Technological University, Singapore.
E-mail: bidesh.sengupta@ntu.edu.sg

Mukesh Kumar Awasthi
Department of Mathematics,
Babasaheb Bhimrao Ambedkar University, Lucknow, India.
E-mail: dr.mukesh@bbau.ac.in

Vinesh Kumar
Department of Computer Science,
Bharati College, University of Delhi, New Delhi, India.
E-mail: vineshjnu@gmail.com

(Received on October 9, 2023; Revised on October 25, 2023; Accepted on November 4, 2023)

Abstract
This article investigates the effects of Atwood numbers on the flow physics of shock-driven elliptical gas inhomogeneity based on numerical simulations. We examine five different gases—He, Ne, Ar, Kr, and SF_6—that are filled inside an elliptical bubble and surrounded by N_2 in order to study flow physics. A high-order modal discontinuous Galerkin finite element approach is used to solve compressible Euler equations for all numerical simulations. In terms of validation studies, the numerical outcomes match the existing experimental data quite well. The findings show that the Atwood number has a significant impact on the characteristics of flow, including wave patterns, the development of vortices, the generation of vorticity, and bubble deformation. When the value of A_t is greater than zero i.e. $A_t > 0$, there is a notable divergence between the incident wave outside the bubble and the transmitted shock wave inside the bubble. Complex wave patterns, including reflected and newly transmitted shock, are seen during the encounter. Interestingly, the transmitted shock and incident shock waves move with the same rates at $A_t \approx 0$. While, compared to the incident shock wave, the transmitted shock wave moves more quickly for $At < 0$. The influence of Atwood number is then investigated in depth by looking at the vorticity production at the elliptical interface. Furthermore, in the analysis of vorticity production processes, the important spatial integrated domains of average vorticity, dilatational and baroclinic vorticity production terms, and evolution of enstrophy are extended. Finally, a quantitative research based on the interface qualities delves deeply into the influence of the Atwood number on the flow mechanics.

Keywords- Shock wave, Elliptical bubble, Atwood number, Vorticity generation.

1. Introduction

The impulsive driving of geometrically severe gas-density inhomogeneities by incident shock waves has been extensively investigated over the past almost half-century. The remarkable shock-driven inhomogeneous flows (SDIFs) are distinguished by the active coupling of numerous fluid dynamic processes, such as mixing flows, the creation of vorticities, and interactions between gas interfaces and

shocks (Ranjan et al., 2011; Danaila et al., 2017; Zeng et al., 2018; Singh et al., 2018, Singh et al., 2021a). The generation of baroclinic vorticity on the interface of the inhomogeneity by the incident shock is thought to be the fundamental driving mechanism of the Richtmyer-Meshkov instability in these dynamic processes (Richtmyer, 1960; Meshkov, 1969). Numerous topics, such as compressible turbulence, inertial confinement fusion, supersonic combustion, supernova explosion, and many more, have been the subject of research on the function of SDIFs. Readers interested in a thorough and up-to-date overview of the literature on SDIFs can be referred to the works of Zhou (2017a, b), Daniel (2020), Brouillette (2002), and Zhou et al. (2021).

In the SDIFs investigations, comprehensive experimental, computational, and theoretical studies have provided rich insights into the shock-driven gas bubbles. Haas and Sturtevant (1987) studied the flow physics of shock-driven cylindrical bubbles with heavy and light gas interfaces. Jacobs (1992, 1993) used experimental research on the interplay of cylindrical gas bubbles and weak shock waves to successfully visualize flow at a higher quality. Using shock tube experiments, Ranjan et al. (2008) studied the flow mechanism of shocked spherical bubble filled with light and heavy gases. Later, Si et al. (2012) and Zhai et al. (2012) conducted experimentally important studies on planar shock interactions at a cylindrical/spherical density interface using high-speed Schlieren photography. Generally, a dimensionless quantity known as the Atwood number, defined by $A_t = (\rho_2 - \rho_1)/(\rho_2 + \rho_1)$ is typically used in a multiphase flow to depict the flow mixing between the gas interface and the surrounding gas. In the above-mentioned expression, ρ_1 is the density of surrounding gas, while ρ_2 denote the density of the interface gas. The shock-driven inhomogeneous flows exhibit distinct flow structure evolutions when different gases with varying Atwood numbers are involved. The fundamental mechanisms governing shock-driven inhomogeneous flows remain consistent in terms of instabilities, vortex formation, shock interaction, while the turbulent mixing, the specific behavior and evolution of these mechanisms can vary with the Atwood number. The Atwood number influences the growth rate of instabilities, the intensity of mixing, the structure of vortices, and the timing of transitions from laminar to turbulent flow. Understanding these variations is essential for predicting and controlling the behavior of such flows in different applications. In order to determine the effect of the Atwood number on the shocked cylindrical bubble, Haehn et al. (2012) experimentally investigated two different values of this property. Zhu et al. (2019) performed numerical simulations of the shocked spherical gas bubble at different Atwood numbers. Recently, Singh et al. (2021a, b) investigated the shocked hydrodynamic instability at the light/heavy cylindrical interface at three distinct Atwood numbers in the context of thermal nonequilibrium circumstances for non-monatomic gases using numerical simulations.

However, all the previously stated experimental and numerical SDIFs research focuses on the interactions between shock waves and circular/spherical bubbles. However, in practical applications, the majority of bubbles turn non-circular when they approach a wall or come into contact with an external force field. In this context, some studies are conducted on the shocked-driven polygonal gas bubbles because the constant incident angle at the interface edge may provide the optimal conditions for the shock-refraction process (Zhai et al., 2014; Luo et al., 2015; Igra and Igra, 2020). Such SDIFs research could potentially have several beneficial uses, such as cavitation erosion, shock wave lithotripsy in medical therapy, ultrasonic cleaning, and volcanic eruption predictions. Motivated by these researches on SDIFs, Singh and colleagues investigated the shock-induced square/rectangular density inhomogeneity through numerical simulations, taking into account multiple factors such as Atwood numbers, shock wave intensities, aspect ratios, coupling impact, and thermal non-equilibrium behavior of non-monatomic gases (Singh, 2020; Singh and Battiato, 2022; Singh and Torrilhon, 2023; Singh, 2023; Singh and Battiato, 2023; Singh and Jallelii, 2023).

Fascinatingly, a variety of theoretical and practical research on the flow field mechanism of shock-driven gas bubbles in various forms has been carried out. A few investigations are conducted to study the flow physics of elliptical bubbles driven by shock waves in non-monatomic gas medium, which is commonly found in the ignition process of inertial confinement fusion and the combustion process in scramjet. Furthermore, the flow physics of shock-driven one or two types of elliptical gas bubbles is the primary focus of these earlier investigations. Moreover, the effects of the Atwood number on the flow physics in shock-driven elliptical bubble have not been thoroughly analyzed, especially from the perspective of quantitative analysis, even when the shock waves interacting with elliptical bubbles filled with different kinds of gases are taken into consideration. Notably, Atwood number is often associated with shock-driven interface flows, such as Richtmyer-Meshkov and Rayleigh-Taylor instabilities, its practical applications extend beyond these specific phenomena.

Here are some practical applications of different Atwood numbers in aerospace engineering (such as, inertial confinement fusion (ICF), aircraft design), meteorology (such as, atmospheric fronts, hurricane and cyclone dynamics), nuclear engineering (such as, nuclear safety), chemical and process engineering (such as, chemical reactors, pharmaceuticals and biotechnology) and many more. For example, in ICF research, the Atwood number is crucial for understanding and controlling the behavior of fuel capsules and implosions. It influences the growth of instabilities, which can impact the success of fusion reactions. Therefore, the current study examines the effects of the Atwood number on the flow physics of shock-driven elliptical gas inhomogeneity, both qualitatively and quantitatively. These values are $A_t = -0.773$, -0.218, 0.074, 0.466, and 0.667 corresponding to He, Ne, Ar, Kr, and SF_6 gases in N_2 gas, respectively. For the numerical simulations, a high-resolution grid and the high-order DG method are used. The rest of this study is structured as follows: Section 2 provides the present problem setup. Section 3 illustrates the computational procedure, including the governing equations, computational approach, and validation study. Section 4 discusses the numerical results to explore the Atwood number effect on the shock-driven elliptical gas bubble. Finally, section 5 draws conclusion on the current investigation.

2. Problem Setup

The computational configuration of the shock-driven elliptical gas inhomogeneity is illustrated in Figure 1. For the computational domain, a rectangular measuring by 150×50 mm^2 is selected. In this configuration, an x-directed shock wave traveling with strength of Mach number $M_s = 1.25$ from the left to the right sides collides with a stationary oblate elliptical bubble. The major and minor axes of the considered elliptical bubble are chosen as a=20 mm, and b=10 mm, respectively. The initial temperature and pressure are taken to be $T_0 = 298$ K and $P_0 = 101{,}325$ Pa, respectively, around the elliptical interface. Nitrogen (N_2) is thought to represent the ambient gas of the elliptical bubble, while five tested gases— helium (He), argon (Ar), sulfur hexafluoride (SF_6), krypton (Kr), and neon (Ne)—are inside the oblate elliptical bubble and are investigated to examine the influence of the Atwood numbers. The properties of the considered gases are shown in Table 1. The upper, bottom, and right boundaries represent the outflow in the computational domain, whereas the left boundary is referred to as the inflow. The numerical simulation is initiated by using the ambient state on the right side of the shock wave, and the primitive variables at the left side of the shock wave are determined by help of the Rankine-Hugoniot criteria (Singh, 2023).

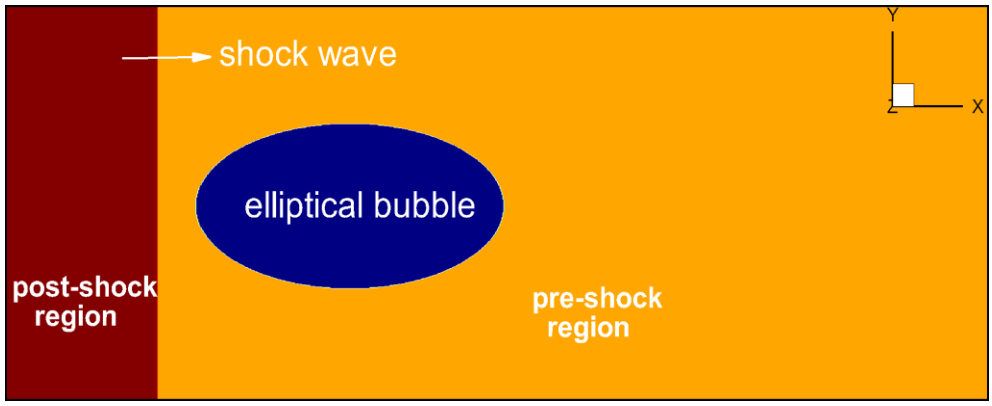

Figure 1. Computational configuration of shock-driven elliptical gas inhomogeneity.

3. Computational Procedure

3.1 Governing Equations

The current study also uses a two-dimensional system of compressible Euler equations to simulate two-component gas flows, building on the prior investigation on shock-driven interface gas inhomogeneity (Singh, 2022; Singh and Torrilhon, 2023). The mechanisms of shocked acceleration, vorticity formation, and mixing are examined independently in this computational setup, whereas the effects of surface tension, reactions, viscosity, ionization, and interactions between numerous inhomogeneities are believed to be minimal and hence ignored. Notably, the selected shock limitation and discretization serve as a source of dissipation to constrict the range of scales. The conservative form of the resulting equations is given as,

$$\frac{\partial \rho}{\partial t} + \frac{\partial (\rho u)}{\partial x} + \frac{\partial (\rho v)}{\partial y} = 0,$$

$$\frac{\partial (\rho u)}{\partial t} + \frac{\partial (\rho u^2 + p)}{\partial x} + \frac{\partial (\rho uv)}{\partial y} = 0,$$

$$\frac{\partial (\rho v)}{\partial t} + \frac{\partial (\rho uv)}{\partial x} + \frac{\partial (\rho v^2 + p)}{\partial y} = 0, \tag{1}$$

$$\frac{\partial (\rho E)}{\partial t} + \frac{\partial ((\rho E + p)u)}{\partial x} + \frac{\partial ((\rho E + p)v)}{\partial y} = 0,$$

$$\frac{\partial (\rho \phi)}{\partial t} + \frac{\partial (\rho u \phi)}{\partial x} + \frac{\partial (\rho v \phi)}{\partial y} = 0$$

where, ρ is the density; u and v are the velocity components in the $x-$ and $y-$ directions, respectively; E is the energy, ϕ is the mass fraction; and p is the pressure which is evaluated from the mathematical expression as follows:

$$p = \gamma_{max} \left(\rho E - \frac{1}{2}(u^2 + v^2) \right) \tag{2}$$

In this context, γ_{max} represents the mixture's specific heat ratio. The equation that describes the relationship between pressure (p), density (ρ), temperature (T), and the mixture-specific gas constant (R) is given is $p = \rho RT$. The assumption is made that both gas components are in thermal equilibrium and behave as calorically perfect gases. These gases are characterized by their specific heats at constant pressure (C_{p1},

C_{p2}), specific heats at constant volume (C_{v1}, C_{v2}), and specific heat ratios (γ_1, γ_2). The specific heat ratio of a mixture can be evaluated by,

$$\gamma_{max} = \frac{C_{p1}\phi + C_{p2}(1-\phi)}{C_{v1}\phi + C_{v2}(1-\phi)} \tag{3}$$

where, subscripts 1 and 2 denotes for bubble and ambient gas, respectively. Remarkably, in numerical experiments, spurious oscillations can be caused by the jump in the specific heat ratio across an interface, especially in issues involving compressible flow. Adaptive strategies, artificial viscosity, boundary conditions, and careful numerical method selection are frequently needed to address this problem and reduce or eliminate oscillations while preserving simulation accuracy.

Table 1. Properties of the selected gases.

Selected gas	Density $(\rho, kg/m^3)$	Specific heat ratio (γ)	Sound speed $(c, m/s)$	Acoustic impedance $(Z = \rho c, Pa\ s/m)$	Atwood number (A_t)
He	0.16	1.66	1007	161	-0.773
Ne	0.80	1.03	452	362	-0.218
N_2	1.25	1.40	352	401	Ambient
Ar	1.45	1.66	319	462	0.074
Kr	3.43	1.66	222	761	0.466
SF_6	6.03	1.09	135	814	0.667

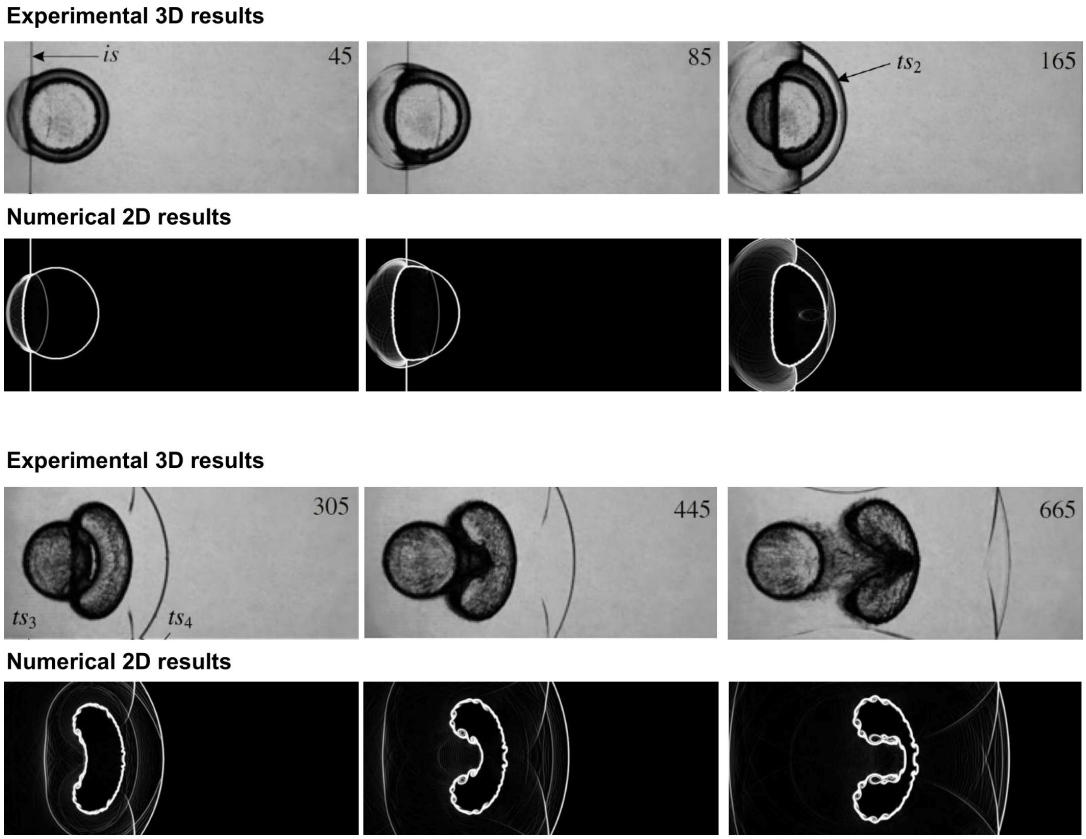

Figure 2. Validation study: comparison between experimental and present results for the shock-driven light cylinder.

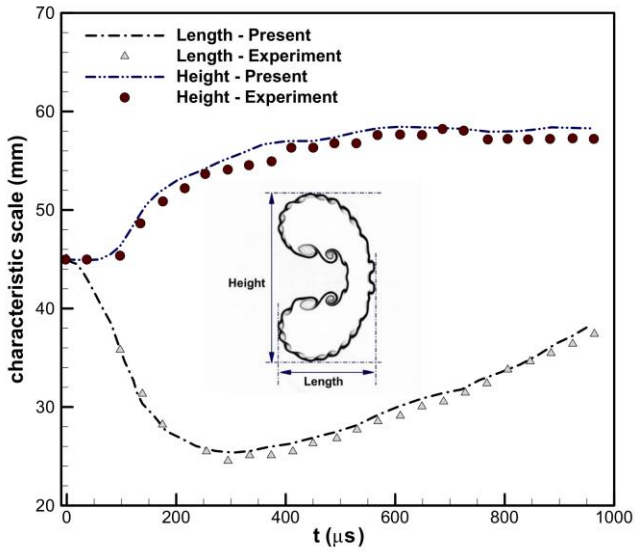

Figure 3. Validation study: comparison of evolving interfaces between experimental and present results for the shock-driven light gas cylinder.

3.2 Computational Method

In the last several decades, discontinuous Galerkin (DG) method has become ubiquitous for the solution of intricate partial differential equation systems in a wide range of domains, including computational biology, quantum physics, plasma physics, fluid dynamics, and multiphase flows (Karchani, 2017; Singh, 2018; Singh and Battiato, 2021a, b; Singh et al., 2022; Singh et al., 2023; Singh and Msmali, 2023). This method is well-suited to handle complex geometries with structured and unstructured, local conservative nature, stability, and high-order precision. This study employs a high-order modal DG scheme to address the governing equations of two-component gas flows, as detailed by Singh (2023). To conduct the numerical simulations, the computational domain is partitioned into equally sized rectangular elements. The approach utilizes a third-order DG scheme, employing the first nine hierarchical modal basis functions that are associated with scaled Legendre polynomials. The HLLC Riemann method, which is specifically developed for two-phase flows, is employed to reconstruct numerical fluxes at the elemental interfaces. The numerical integration of the volume and surface integral terms utilizes the Gauss-Legendre quadrature rule. In addition, a highly accurate third-order Runge-Kutta method with Total Variation Diminishing is utilized to solve the differential equations that depend on time. The computational solutions incorporate a moment limiter proposed by Krivodonova (2007) to diminish the occurrence of nonphysical oscillations.

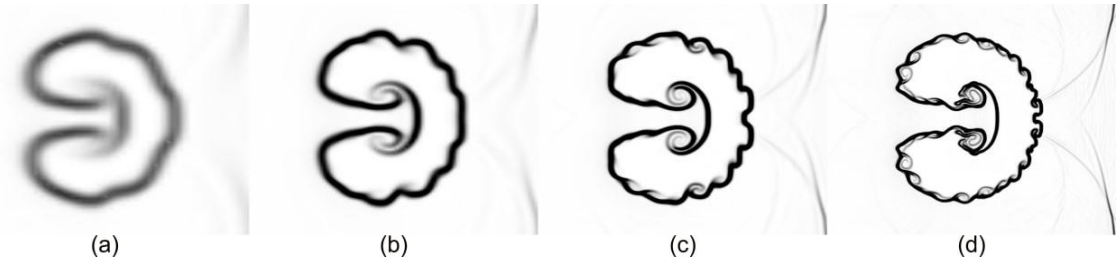

Figure 4. Grid resolution analysis with four different grids (a) 200×100, (b) 400×200, (c) 800×400, and (d) 1200×600 in the shock-driven elliptical He bubble at $\tau = 7$.

3.3 Validations

The present numerical model and associated solver for various light/heavy bubbles with cylindrical and polygonal shapes stimulated by an incoming shock wave have been verified in our earlier research. (Singh, 2020; Singh, 2021a, b; Singh and Battiato, 2022; Singh and Torrilhon, 2023; Singh, 2023; Singh and Battiato, 2023; Singh and Jallelii, 2023). In order to confirm the accuracy of the current numerical solver, we conduct an extra validation using the shocked spherical bubble experiment conducted by Ding et al. (2017). The validation process involves comparing the numerical representation of a shocked cylindrical bubble at a Mach number of 1.29 with the experimental results of a shocked spherical bubble. In this experiment, the bubble is enclosed by SF_6 and contains N_2 gas. Figure 2 illustrates the comparison between the shadowgraph images acquired from both the experimental observations and the numerical simulation results at the selected time instances, demonstrating a strong concurrence between the two. Moreover, Figure 3 demonstrates the temporal evolution of the interfacial characteristic scales for the N_2 cylindrical bubble as the interface undergoes changes. The experimental study conducted by Ding et al. (2017) aligns well with the current numerical findings, indicating a strong correlation between the two.

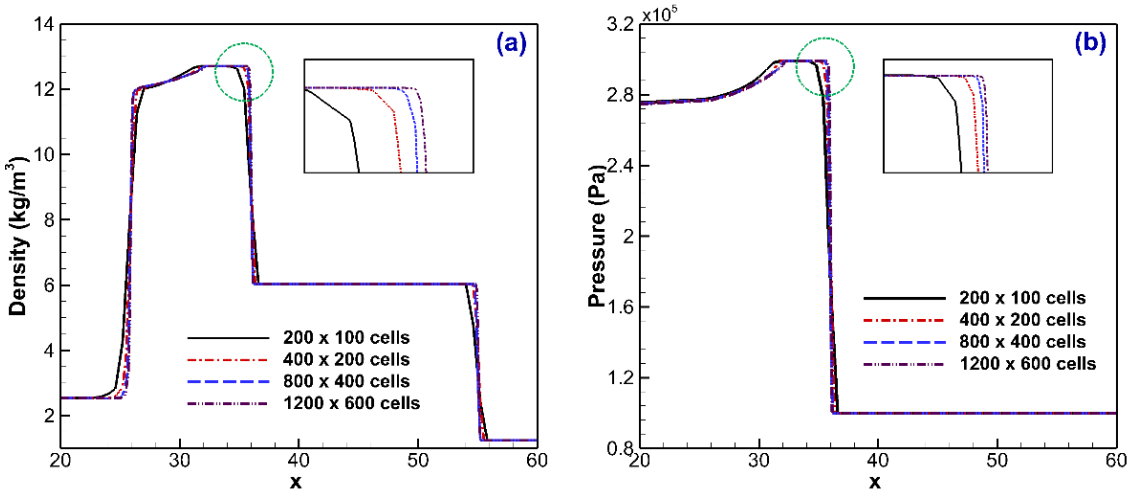

Figure 5. Grid resolution analysis with four different grids: (a) density, and (b) pressure distributions profiles along the centerline of the shock-driven elliptical He bubble at $\tau = 3$.

3.4 Grid Resolution Analysis

All subsequent experiments assume a dimensionless timescale (τ) provided by a computational flow time:

$$\tau = t.\frac{c.M_s}{max(a,b)} \tag{4}$$

where, a and b represent the major and minor axes lengths of the oblate elliptical bubble, respectively, and c and t represent the local sound speed and real-time sound speed, respectively.

For the grid resolution analysis, one test case of shock-driven elliptical bubble is carried out with four different grid refinements, including 200×100, 400×200, 800×400, and 1200×600 grid points. As seen in Figure 4, the diverging shape is produced when the incident shock wave completely compresses the volume of the elliptical bubble at $\tau = 7$. Furthermore, the flow field generates two major vortex rings. The KH instability is observed in terms of rolled-up small-scale vortices on the bubble interface, which is one of the primary variances between the four testing examples. As the grid fineness rises, the interface gets

sharper and the KH instability at the interface is more apparent. The density and pressure distribution profiles along the computer elliptical bubble's centerline at $\tau = 3$ are displayed in Figure 5. The findings show that as grid resolution increases, the dissipations of the density and pressure profiles decrease. However, the subsequent computational tests using 1200×600 grid points are carried out to ensure enough numerical precision while conserving computer resources.

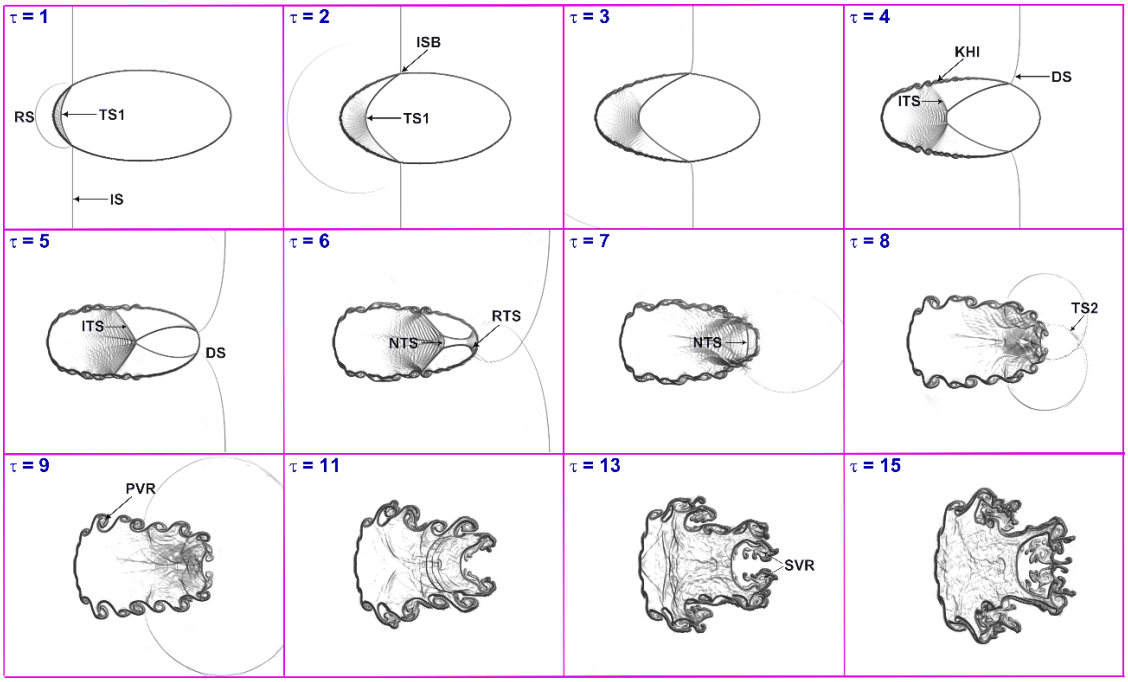

Figure 6. Flow structure evolution for the shock-driven elliptical SF_6 bubble at $A_t = 0.667$.

4. Results of Atwood Effect on Shock-Driven Elliptical Gas Bubble, and Discussion

This section discusses how the flow physics of shock-driven elliptical gas bubble is affected by the Atwood number. Particular attention is paid to the effects of initial interface disturbance on the distribution of vorticity, flow morphology, wave patterns, interface features, and qualitative analysis. For the numerical simulation, the shock wave with $M_s = 1.25$ is taken into consideration. Based on the density gradient field magnitude, we employ numerical schlieren pictures to study the impact of Atwood numbers on the shock-driven elliptical gas bubble.

$$S_{i,j} = exp\left(-k(\phi_{i,j})\frac{|\nabla\rho_{i,j}|}{max_{i,j}|\nabla\rho_{i,j}|}\right) \tag{5}$$

where, $k(\phi_{i,j}) = \begin{cases} 20 & if\ \phi_{i,j} > 0.25 \\ 100 & if\ \phi_{i,j} < 0.25. \end{cases}$

4.1 Visualization of Flow Structure

The phenomena of visualizing the flow structure in shock-driven inhomogeneous flows is said to be the most fascinating one. Here, we carried out in-depth studies of the flow structure evolution for the shocked elliptical gas bubble with various Atwood numbers in order to comprehend this phenomenon.

Figure 6 shows the flow structure generated by the shock-driven elliptical SF_6 bubble with $A_t = 0.667$. Due to the higher acoustic impedance, the shock wave inside the elliptical SF_6 bubble travels at a slower pace compared to its propagation in the surrounding medium. As a result, the transmitted shock (TS1) wave within the bubble is far behind the IS wave outside of it. The bubble starts to compress inwards when the IS wave collides the bubble interface. At the same time, a reflected shock (RS) wave travels upstream and the TS1 wave propagates downstream inside the bubble. The compressed volume initially takes the shape of a crescent, and the TS1 wave is initially plainly visible inside the volume and slightly converging. It is also possible to observe the incident shock wave along the bubble interface (ISB), which moves more slowly than the IS wave. The curvature of the TS1 wave increases as the IS wave crosses the bubble interface's top point. It is also seen that the top and bottom ends of the two straight sections of the IS wave are related to a curved diffracted shock (DS) wave outside the bubble. Remarkably, in the course of this procedure, one novel inner transmitted shock (ITS) is discovered. As the IS wave passes through the outer bubble, the curved TS1 constantly pushes it back. Later, outside the bubble, the ends of the DS wave that connected to the IS wave are severely deformed. A portion of the bubble-ambient gas interface is seen to be thicker behind the TS1 wave than it is in front of it when it crosses the bubble. The Kelvin-Helmholtz instability (KHI) is responsible for the roll-up of small-scale vortices. As the DS and TS1 waves converge over time, a shock-focusing zone is formed toward the downstream end point of the bubble on its axis. A new transmitted shock (NTS) wave is created when the downstream interior bubble experiences a simultaneous upstream movement of a reversed transmitted shock (RTS) wave.

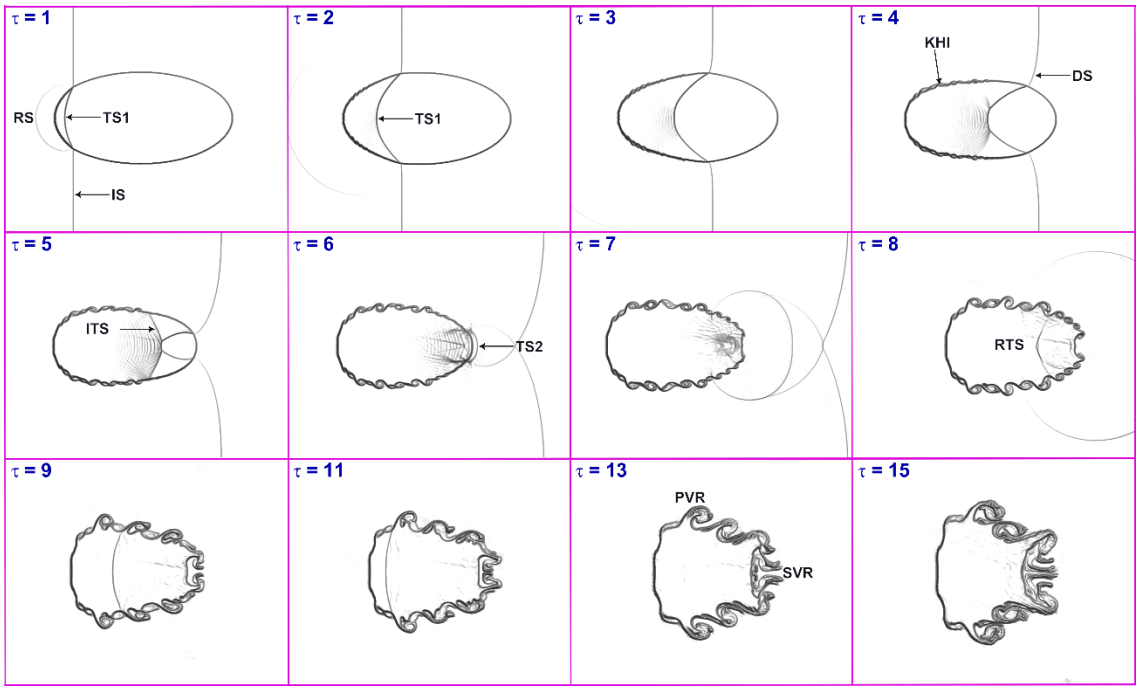

Figure 7. Flow structure evolution for the shock-driven elliptical Kr bubble at $A_t = 0.466$.

Since the elliptical SF_6 bubble has a larger acoustic impedance than the ambient medium, the IS wave propagates more slowly within it. Figure 7 illustrates the flow structure evolution of the shock-driven Kr elliptical bubble in the ambient N_2 gas, which can be studied in more detail in order to examine these discrepancies. In contrast to Figure 6, the transmitted shock (TS1), reflected transmitted shock (RTS), diffracted shock (DS), and other shock configurations are also visible in the frontal region of the elliptical

bubble, along with the reflected shock (RS) wave. The area of the unshocked region in the Kr bubble is lower than in the SF_6 bubble, though, since the shock waves in the Kr bubble travel faster than in the SF_6 bubble due to the smaller acoustic impedance of Kr. The shock wave then focuses, but in contrast to the SF_6 bubble, it does so at a location that is a little closer to the downstream pole of the Kr bubble, and it also occurs at a time that is earlier than expected. At the Kr bubble interface, primary and secondary vortex pairs (PVR and SVR) are created with lower strengths than in the SF_6 bubble scenario. Remarkably, due to the high pressure caused by the shock focusing phenomena, a distinct SVR pattern is seen at the center of the back surface of the Kr bubble. The main tendencies of the Kr and SF_6 elliptical bubbles in the evolution of shock waves and bubble deformation are essentially consistent, despite some specific variances between the two different situations caused by the values of the Atwood number for the Kr and SF_6 gases.

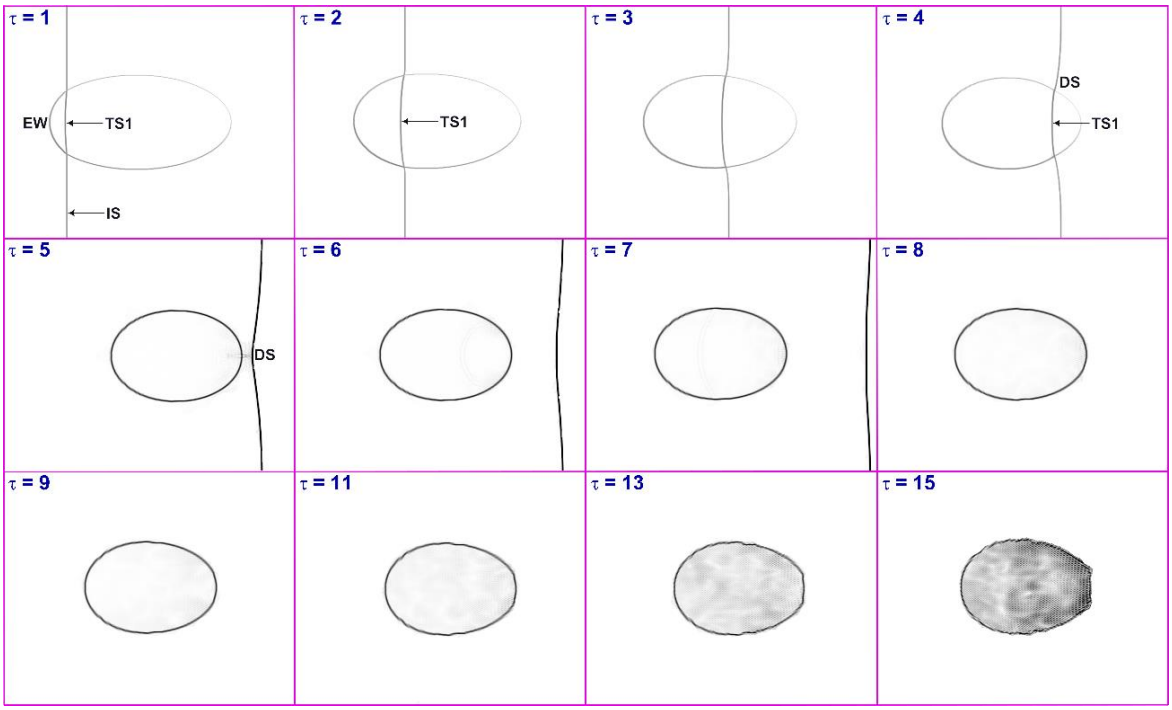

Figure 8. Flow structure evolution for the shock-driven elliptical Ar bubble at $A_t = 0.074$.

The density of Ar, which is slightly higher than that of the surrounding N2, can be distinguished by a positive Atwood number (A_t = 0.074) as the elliptical gas density decreases. This arrangement indicates that the elliptical bubble, propelled by the shock, is in a configuration where it alternates between slow and fast speeds. Figure 8 illustrates the time evolution of flow structure for the shocked elliptical Ar bubble at $A_t = 0.074$**.** The wave pattern in this particular setup would differ from the one previously shown with $A_t = 0.466$ and $A_t = 0.667$ due to the similar acoustic impedance between the gases involved (nitrogen and argon), as expected. It can be noted that the IS and TS1 waves exhibit comparable velocities. During the initial phase of interaction between the IS wave and the square bubble, the TS1 wave travels at a slightly slower speed within the bubble compared to the IS wave outside. This discrepancy arises due to the Ar gas having a slightly lower acoustic impedance than N_2. Simultaneously, it is noted that the interaction between the IS wave and the bubble results in the generation of an expansion wave (EW) close to the left interface of the elliptical bubble. The arrival of the TS1 wave inside the Ar bubble at its rear surface coincides with the arrival time of the IS wave at the same location. After the TS1 shock wave travels to the rear surface of

the elliptical bubble, it transmits a shock wave into the surrounding N_2 gas. Simultaneously, an internal shock wave, known as a reflected transmitted shock (RTS) wave, is produced within the bubble. The reflected transmitted shock (RTS) wave leaves the bubble through its front surface and moves in the opposite direction, upstream, into the ambient gas. It is worth noting that the weak shock wave generated from the frontal surface of the initial elliptical bubble does not result in the formation of a vortex ring at the front of the bubble. Nevertheless, the front surface of the bubble appears somewhat level throughout the observed period.

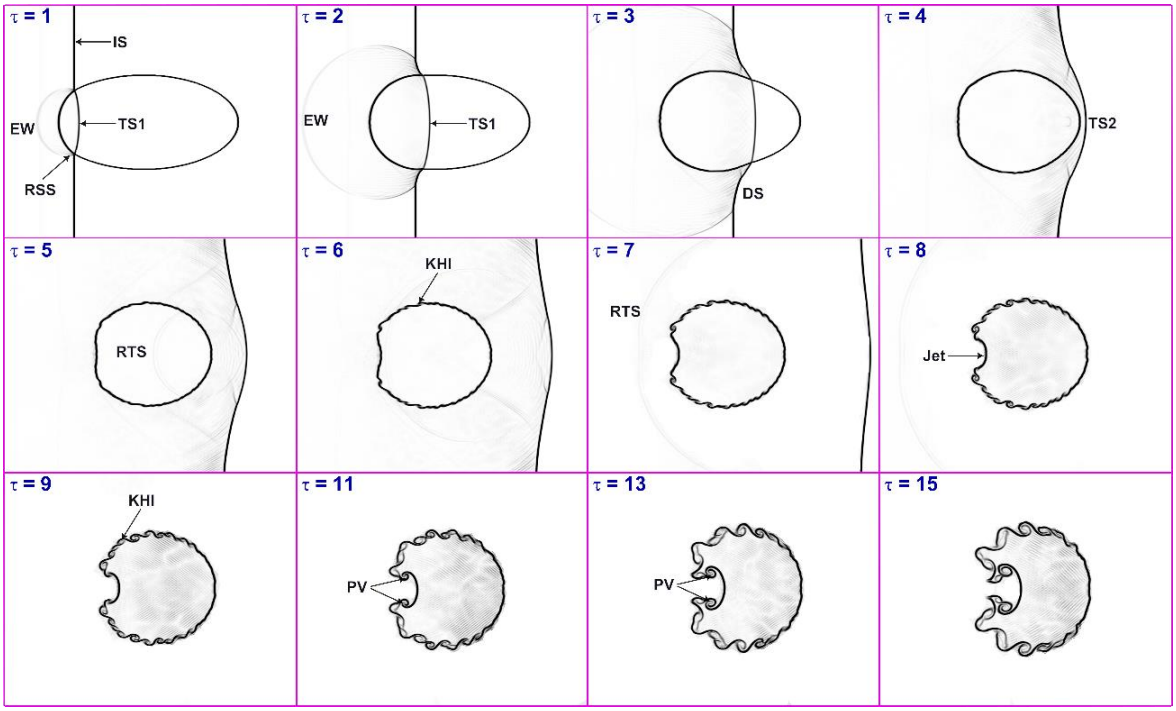

Figure 9. Flow structure evolution for the shock-driven elliptical Ne bubble at $A_t = -0.218$.

The evolution of flow structure for the elliptical Ne bubble driven by shock at $A_t = -0.218$ is presented in Figure 9. When the IS wave first encounters the elliptical bubble, the speed at which the transmitted shock (TS1) wave travels within the bubble are significantly greater than that of the IS wave outside the bubble. This is due to the slightly lower acoustic impedance of Ne gas compared to nitrogen gas. Simultaneously, it is noted that the collision between the IS and bubble generates a reflected rarefaction shock (RRS) and expansion wave (EW) in close proximity to the interface of the left bubble. As the interaction between the shock wave and the Ne elliptical bubble continues, the bubble begins to compress, resulting in a somewhat level appearance of the left interface. Similar to the He case, when the first transmitted shock wave (TS1) impacts the back surface of an elliptical bubble, it sends a shock wave (TS2) into the surrounding nitrogen gas, resulting in the creation of a reflected transmitted shock wave (RTS). Following that, the TS2 wave combines with a linear surface ahead of the bubble, whereas the RTS emerges from the frontal side of the bubble and continues to move against the flow into the nitrogen gas. Over a period of time, the left side of the bubble undergoes a gradual inward bending, accompanied by a slow curvature of the primary vortex rings (PVR) on the surface.

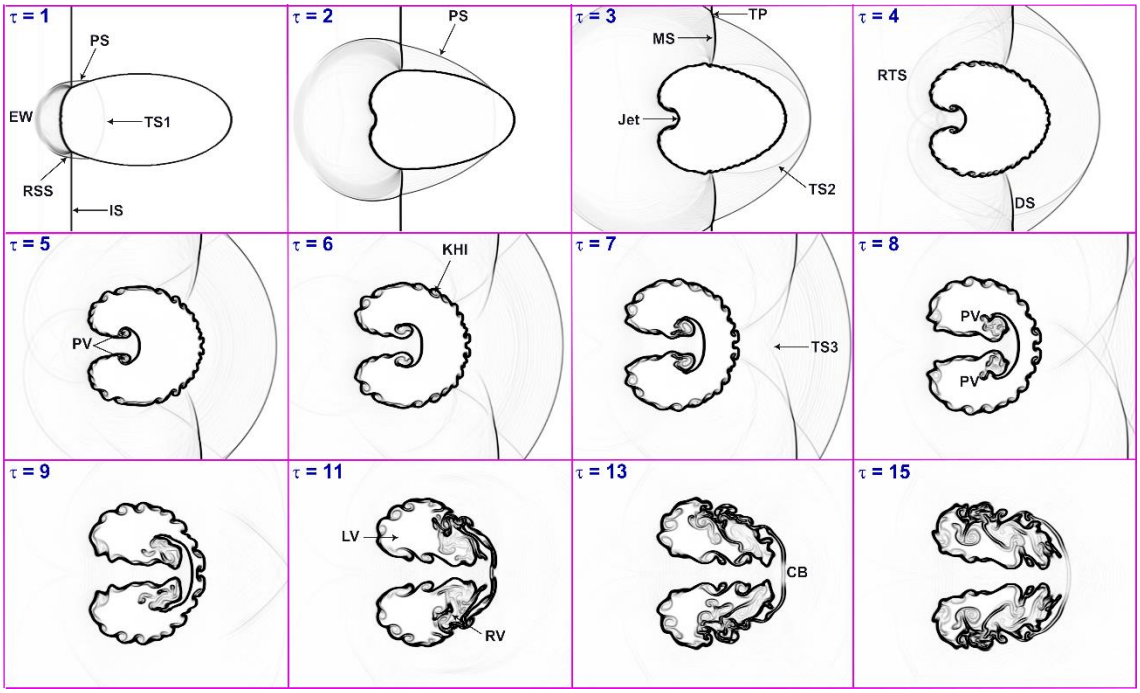

Figure 10. Flow structure evolution for the shock-driven elliptical He bubble at $A_t = -0.773$.

Figure 10 depicts the evolution of the flow structure over time in an elliptical He bubble driven by a shock wave, with $A_t = -0.773$**.** The speed at which the incident shock wave travels within the elliptical helium bubble is greater than that of the surrounding medium because of its lower acoustic impedance (i.e., Z = 161 Pa s/m). The shock wave that is transmitted within the bubble is positioned far behind the shock wave that exists outside the bubble. The compression of the bubble commences as soon as the IS wave reaches the bubble interface. Furthermore, the elliptical He bubble generates a transmitted shock wave (TS1) that moves downstream. At the same time, an expansion wave (EW) and a reflected rarefaction wave (RRS) travel upstream. The TS1 undergoes refraction upon reaching the bubble interface, causing it to emit a new shock wave called the precursor shock (PS) at an oblique angle into the surrounding gas. As the interaction progresses, the incident shock and transmitted shock waves combine to create a fourfold shock pattern in the surrounding gas, exhibiting irregular refraction. As a result, the formation of a Mach reflection configuration occurs, comprising of a Mach stem (MS) and triple point (TP). Subsequently, a secondary shock wave (TS2) becomes noticeable in the vicinity of the interface downstream. Also, a shock wave known as the reflected transmitted shock (RTS) wave is generated within the helium bubble, originating from the upstream surface and currently propagating in the opposite direction towards the front of the bubble. In addition, a shock wave that has undergone diffraction (DS) moves along the boundary of the bubble. The vorticity arises on the bubble interface because of the baroclinic effect, leading to an inward air jet from the bubble's surroundings. As a result, the left side of the bubble interface, which was previously flattened, starts to move inward. Over time, the vorticity gradually gives rise to a compact vortex pair (V), which exhibits a counterclockwise rotation in the upper portion of the distorted helium bubble. Subsequently, a secondary shock wave (TS2) becomes noticeable in the vicinity of the interface downstream. At the same time, the incident shock (IS), reflected transmitted shock (RTS), and diffracted shock (DS) combine to form a flat shock, leading to an increase in complexity of the flow patterns close to the interface downstream. Over time, the helium bubble that has been distorted gives rise to two large vortex pairs (referred to as LV and RV). In our previous study (Singh et al., 2021), we observed that the difference

in area between the LV and RV is less pronounced in the elliptical helium bubble case. This finding highlights the distinction between the elliptical and cylindrical cases, underscoring the importance of our current study. Eventually, the jet reaches the downstream bubble interface, resulting in the emergence and almost symmetrical growth of a pair of vortex rings (LV, RV) that are linked by a bridge (CB). Over time, the vortex rings take full control of the flow field.

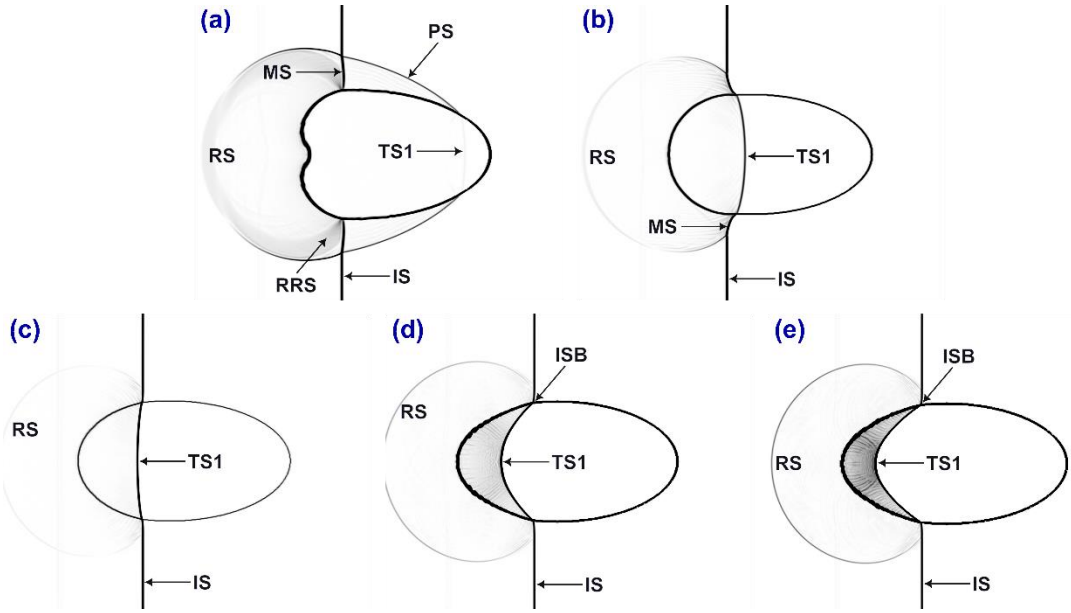

Figure 11. Effect of Atwood number on the flow structures at $\tau = 3$: (a) $A_t = -0.773$ (He), (b) $A_t = -0.218$ (Ne), (c) $A_t = 0.074$ (Ar), (d) $A_t = 0.466$ (Kr) and (e) $A_t = 0.677$ (SF_6).

Figure 11 depicts the comparative examination of the flow pattern in the shock-driven elliptical bubble at various Atwood numbers during the initial stages when $\tau = 3$. The density and acoustic impedance play a crucial role in determining the deformation of the elliptical bubble during the penetration of the shock wave for different Atwood numbers. The He and Ne gases exhibit the greatest penetration speed, surpassing that of the regular IS wave. In both instances, the elliptical bubbles experience a faster passage of the transmitted shock compared to the incoming shock wave beyond the boundary of the bubbles. The speed of the transmitted wave within the elliptical bubble is slower in helium compared to neon. Surprisingly, the scenario changes when considering the Ar elliptical bubble, as the slight disparity in the speeds of transmitted shock and incoming shock waves leads to a lesser distortion of the bubble. Conversely, the situation in Kr and SF_6 presents an opposite scenario to that of Ne and He gases. The SF_6 bubble exhibits the slowest penetration speed, which interestingly surpasses the speed of the regular IS wave.

Interestingly, in shock-driven interface flows, the onset and development of KHI are influenced by the Atwood number, which characterizes the density difference between the two fluids, and by differences in acoustic impedance, which can affect pressure gradients and the overall stability of the interface. A larger Atwood number and significant differences in acoustic impedance can enhance KHI and lead to the formation of more pronounced vortices and turbulent mixing. The specific behavior of KHI in different gas-gas interfaces would require detailed numerical simulations or experimental studies, as the outcomes can vary depending on the exact properties of the gases involved. Understanding the role of variations in acoustic impedance among different gases, along with their respective Atwood numbers, in the context of

Kelvin-Helmholtz instabilities (KHI) and shock-induced flow behaviors is crucial in several applications, particularly in the field of fluid dynamics, aero- and hydrodynamics.

4.2 Vorticity Transport Equation and Associated Flow Physics

By carefully analyzing the components within the vorticity transport equation (VTE), one can enhance their comprehension of the processes involved in the dynamics of vortices. The VTE can be expressed for compressible inviscid flows as:

$$\frac{D\omega}{Dt} = (\omega.\nabla)\boldsymbol{u} - (\nabla.\boldsymbol{u})\omega + \frac{1}{\rho^2}\nabla\rho \times \nabla p \tag{6}$$

The vorticity transport equation involves several variables, namely vorticity (ω), velocity ($\boldsymbol{u}$), density (ρ), and pressure (p), which collectively describe the flow field. The left-hand side of the equation represents the material derivatives, encompassing the unsteady ($\partial\omega/\partial t$) and convection ($\boldsymbol{u}.\nabla)\omega$ terms. On the right-hand side, the first term characterizes vorticity stretching caused by velocity gradients, becoming negligible in turbulent and two-dimensional mixing flows. The second term accounts for vorticity stretching due to flow compressibility. The third term signifies the creation of small-scale vortices at the bubble surface, known as baroclinic vorticity production, which is particularly significant in shock-driven interface flows due to the disparity between density and pressure gradients.

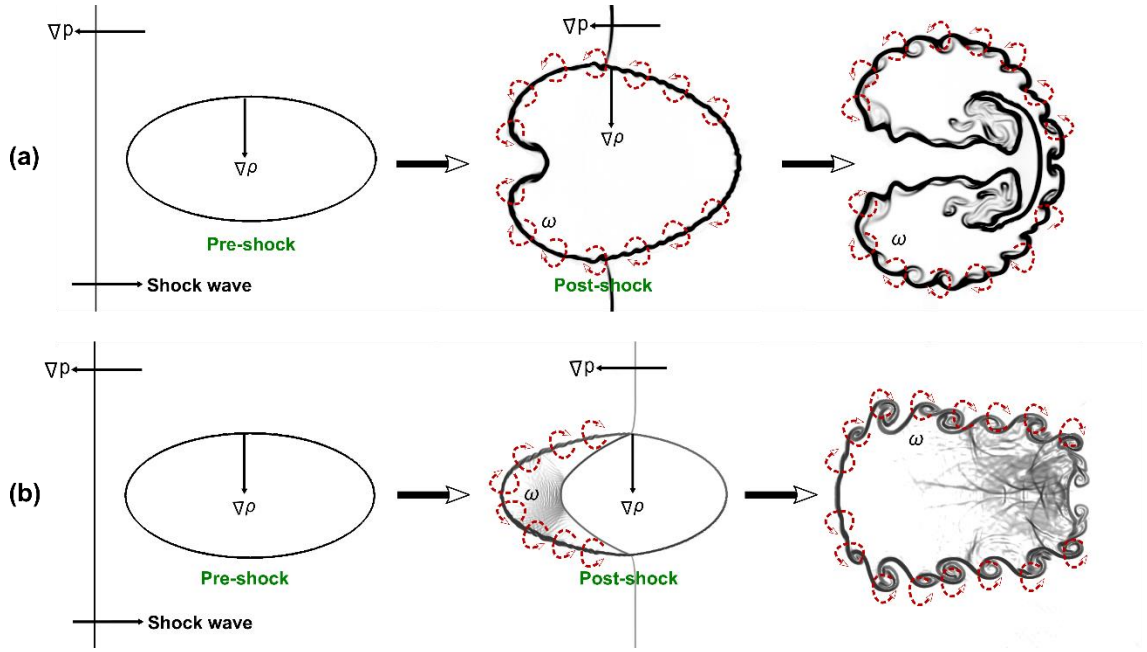

Figure 12. Diagram of vorticity generation process in (a) light gas interface, and (b) heavy gas interface.

The generation and distribution of baroclinic vorticity occur as the IS wave moves through the elliptical gas. This process primarily takes place at the interface of the elliptical region, where density gradients are present. The misalignment between the density gradient ($\nabla\rho$), and the pressure gradient (∇p) results in the generation of baroclinic vorticity. This misalignment significantly affects the development of hydrodynamic instability. Figure 12 displays the schematic representation of the generation of vorticity within an elliptical bubble driven by a shock wave, which is filled with either a light or a heavy gas. A rolled-up vortex is generated at the leftmost elliptical interface when the incident shock contacts the

perfectly aligned pressure and density gradients, creating a small amount of vorticity. The incident shock wave travels along the top horizontal interface, resulting in an uneven reflection where the Mach stem links the shock wave with the elliptical interface. Hence, the Mach stem generates the pressure gradient that leads to the development of vorticity on the interface. Consequently, the baroclinic vorticity component is gradually activated as the incident shock moves upward across the elliptical interface. Surprisingly, the formation of rolled-up vortices is less prominent at the downstream end of a heavy gas bubble interface as compared to the downstream end of a light gas bubble interface.

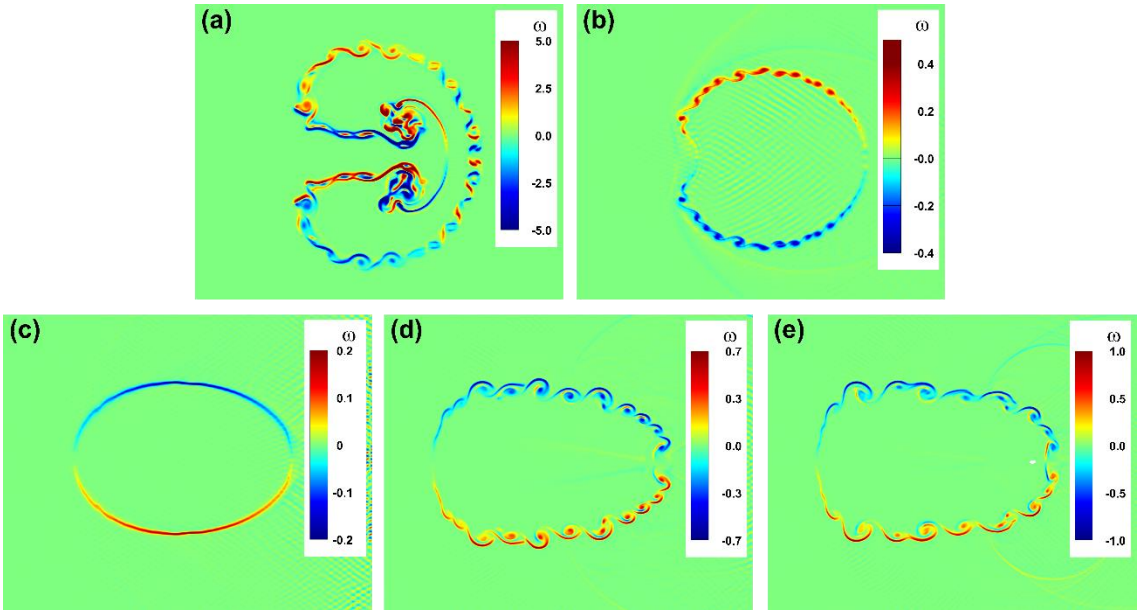

Figure 13. Effect of Atwood number on vorticity generation at the same time instant $\tau = 8$: (a) $A_t = -0.773$, (b) $A_t = -0.218$, (c) $A_t = 0.074$, (d) $A_t = 0.466$, and (e) $A_t = 0.667$.

Figure 13 illustrates how the Atwood number influences the generation of vorticity in the shock-driven elliptical bubble at the specific time $\tau = 8$. After the interaction, noticeable variations in the distribution of vorticity can be observed among different Atwood numbers. When the Atwood number is negative ($A_t < 0$), vorticity is produced on the upper side of the bubble interface, resulting in positive vorticity. On the other hand, the lower side of the interface generates negative vorticity. This can be observed in Figures 13(a) and 13(b). The reason for this is the propagation of the shock wave moving in a rightward direction across the interface of the bubble. Consequently, the density gradient extends outward in a radial manner at the interface of the bubble, while the pressure gradient exists along the upstream shock wave. Moreover, the upper interface exhibits a vortical configuration characterized by positive vorticity at its core, accompanied by negative vorticity tails. Conversely, the lower interface of the elliptical bubble displays the opposite scenario. When the Atwood number is approximately zero, specifically at $A_t = 0.074$, it can be observed that there is an absence of vorticity generation in the vertical interfaces located on the leftmost and rightmost sides of the elliptical bubble. In the case of a positive Atwood number ($A_t > 0$), an intriguing observation is that both negative and positive vorticity are generated on the upper and lower interfaces of the elliptical bubble. This phenomenon can be clearly seen in Figures 13(d)-(e). The upper and lower interfaces of the elliptical interface contain a substantial level of vorticity. Following shock focusing, the distorted shock wave generates a minor amount of both negative and positive vorticity on the upper and lower interfaces. The prevailing positive (negative) vorticity is also concentrated on the upper-half (lower-

half) plane within the inward jet. The higher amplitude attenuation of the deformed shock wave at the downstream pole of the bubble may potentially explain the concentration of dominant positive (negative) vorticity in the upper-half (lower-half) plane of the outward jet head. The presence of positive (negative) vorticity on the upper (lower) jet head facilitates the inward movement of the jet, indicating the connection between the formation of the jet and the generation of vorticity. In summary, the Atwood number directly influences vorticity generation and mixing in flows involving two different gases. Variations in Atwood number lead to differences in the intensity of vortical structures and the efficiency of mixing. These principles can be generalized and applied to a wide range of flow configurations and geometries, making them valuable tools for optimizing mixing processes and flow control in various applications across engineering and science.

At this point, it is necessary to discuss the important spatially integrated fields, which can help us for further understanding of vorticity production phenomena. These quantities are the following – average vorticity (ω_{av}), dilatational vorticity production $(P_{\omega,dil})$, and baroclinic vorticity production $(P_{\omega,baro})$. The mathematical expression of these spatially integrated fields is given as,

$$\omega_{av}(\tau) = \frac{\int |\omega| dxdy}{\int dxdy} \tag{7}$$

$$P_{\omega,dil}(\tau) = -\frac{\int |\omega(\nabla.\boldsymbol{u})| dxdy}{\int dxdy} \tag{8}$$

$$P_{\omega,baro}(\tau) = \frac{\int \left|\frac{1}{\rho^2}\nabla\rho\times\nabla p\right| dxdy}{\int dxdy} \tag{9}$$

Figure 14 displays the spatial integrated fields of average vorticity, dilatational and baroclinic vorticity productions in shock-driven elliptical bubbles with different Atwood numbers. Vorticity at its interface can have a major role in influencing the gas mixing both inside and outside of the elliptical bubble. To put it more precisely, the average vorticity experiences an increment as a result of the interaction of the incident and reflected shock waves with the elliptical bubbles. The intensified vorticities aid in the mixing of gases inside and outside the gas bubble, thereby facilitating the transfer and utilization of vorticity energy, which may eventually result in a gradual reduction in the average vorticity intensity in the bubble area. Nonetheless, the average vorticity usually increases because of the more robust development of the RM instability as the Atwood number increases. Interestingly, the largest average vorticity is observed at highest positive Atwood number i.e., $A_t = 0.667$, as shown in Figure 14(a). On the other hand, the dilatational and baroclinic vorticity production terms associated with the generation of vorticity exhibit considerable magnitudes when they interact and decrease soon after they pass through the IS wave. In Figure 14(b), the dilatational vorticity production term displays the occurrence of compressed structures around the vortex core because of compressibility effects that arise from local regions of compression and expansion. One can observe that the smallest value of dilatational production term is found at $A_t = 0.667$, while the largest value is seen at $A_t = -0.773$. In Figure 14(c), the baroclinic vorticity production term reveals the vorticity created by the misalignment of pressure and density gradients, which is caused by the presence of reflected shock structures and interface discontinuity. The collision of the shock wave with the bubble generates vortices that facilitate the mixing of the elliptical bubble with the surrounding gas. During the second impact of the reflected shock waves on the deformed bubble, the spatially integrated fields experience their maximum growth rate, implying a significant increase in vorticity during this phase. Subsequently, the rate of growth in the flow field decreases.

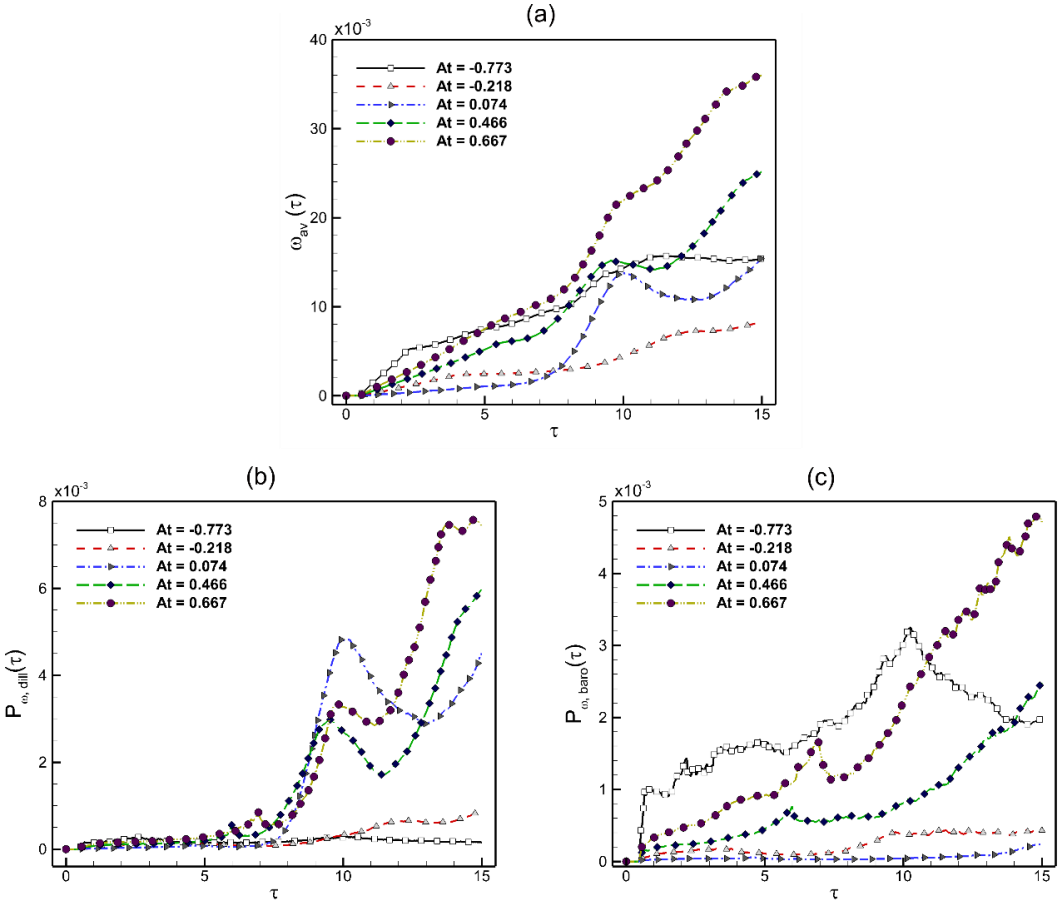

Figure 14. Effect of Atwood number on the spatial integrated fields of (a) average vorticity, (b) dilatational vorticity, and (c) baroclinic vorticity production terms.

4.3 Time Evolution of Enstrophy and Kinetic Energy

Understanding the physical mechanisms of vorticity creation or attenuation during the encounter can be aided by looking at the time evolution of the enstrophy. It is defined as the area in the flow field that is integral to the square of the vorticity.

$$\Omega(\tau) = \frac{1}{2}\iint \omega^2 dxdy \tag{10}$$

In the flow field, the spatial integral of the square of the velocity can be used to define the time evolution of the kinetic energy (K.E.).

$$\text{K. E.}(\tau) = \frac{1}{2}\iint \boldsymbol{u}^2 dxdy \tag{11}$$

In the shock-driven elliptical bubble, Figure 15 shows the Atwood number impacts on the time development of enstrophy and kinetic energy distribution. Following the collision, the kinetic energy and enstrophy at different Atwood numbers differ significantly. Unless the shock wave reaches the bubble's upstream pole, it is zero in the case of enstrophy evolution. Subsequently, the creation of baroclinic vorticity causes it to rise as the shock wave passes. The enstrophy rises at the bubble interface where the incoming shock and reflected shock waves impinge. The heightened vorticities promote the blending of gases both inside and outside the gas bubble, accelerating the exchange and utilization of energy. Consequently, this process

gradually diminishes the magnitude of enstrophy within the bubble region. The all-Atwood numbers exhibit the same phenomena. Interestingly, at the maximum negative Atwood number $A_t = -0.773$, the highest value of enstrophy is seen. To delve deeper into the impacts of the Atwood number, we present visual representations of the cumulative kinetic energy fields over time. The Atwood number influences the kinetic energy's development, which varies. With the Atwood numbers falling, it is evident that the kinetic energy is much increased.

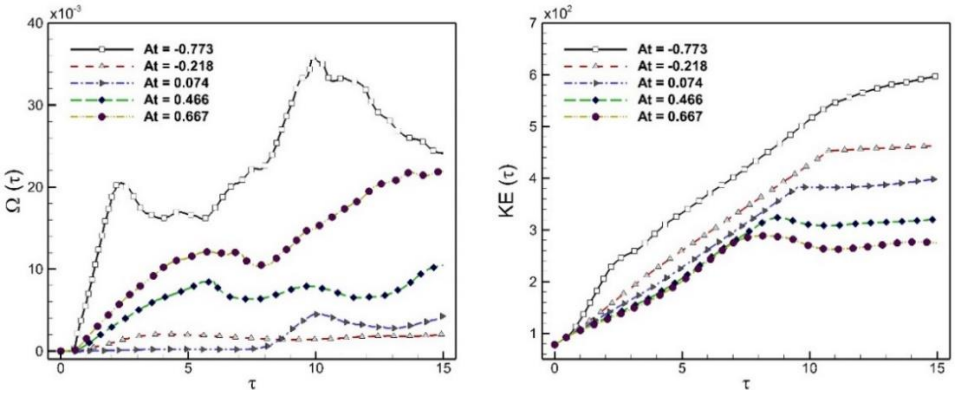

Figure 15. Effect of Atwood number on time evolution of enstrophy, and kinetic energy.

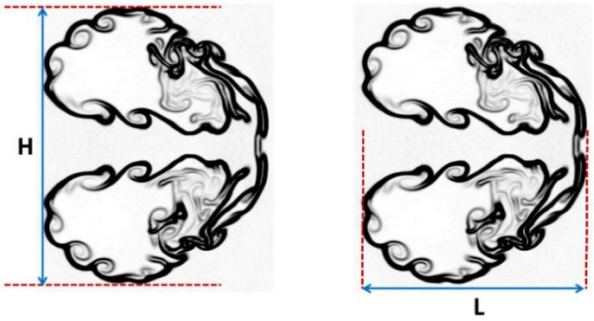

Figure 16. Schematic diagram of the interface characteristics quantities: interface height, and interface length.

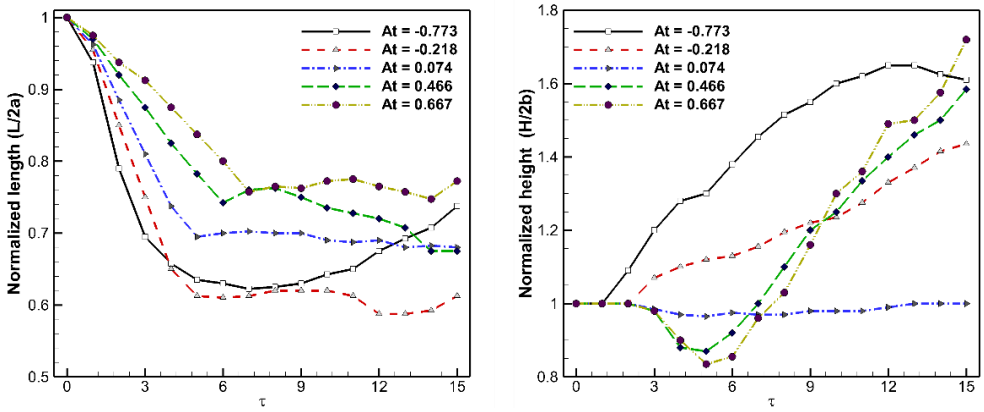

Figure 17. Atwood number effect on the time variations of normalized interface height and length.

4.4 Quantitative Analysis Based on Interface Features

Ultimately, a numerical examination grounded in the interface features is showcased to investigate the Atwood number impacts on the shock-driven elliptical bubbles. Figure 16 illustrates a schematic diagram the interface characteristics quantities such as interface length and interface height. Figure 17 illustrates the effect of Atwood number on the time evolution of the normalized interface length ($i.e. L/2a$), and the normalized interface height ($i.e. H/2b$) for the shock-driven elliptical bubbles. As the incoming shock wave compression collides the bubble during the early stages of interaction, it significantly reduces the length of the growing interface. Afterward, the acceleration of the vorticity-induced velocity causes the inward jet and vortex pair to form in the bubble's upstream interface, causing the bubble width to rise fast. It is interesting to note that all the Atwood number exhibits similar physical features. The interface length remains nearly constant for a considerable amount of time after the compression phase. Then, as the jet and upstream vortex pairs expand, it gradually rises. The interface length gradually reduces for the remaining A_t values before becoming largely constant. However, until the wall-reflected shock waves hit the interface and slow down the interface height growth rate, the interface height rises steadily as a result of the vortex pair's continued rotation. The figure illustrates that the longest interface height is observed at $A_t = 0.667$, and the smallest interface height is recorded for $A_t = = 0.074$.

In summary, the observed variations in vorticity, kinetic energy, and interface deformation with changing Atwood numbers provide valuable information for optimizing the design and efficiency of practical applications, such as supersonic propulsion systems and the prediction and control of turbulence in shock-driven flows. These insights enable engineers and researchers to make informed decisions and improvements in their respective fields.

5. Concluding Remarks

This study investigates the Atwood number influence on the flow physics of shock-driven elliptical gas inhomogeneity via numerical simulations. To delve into the study of fluid dynamics, we examine the behavior of gases within an elliptical bubble, which is filled with five different gases: Neon (Ne), Helium (He), Argon (Ar), Sulfur Hexafluoride (SF_6), Krypton (Kr), and, which are enclosed in a nitrogen (N_2) environment. The focus was directed towards visualizing flow patterns, wave behavior, changes in interface shape and position, vorticity creation, and performing a quantitative analysis. Utilizing the compressible Euler equations for all numerical simulations, these equations were solved using a modal discontinuous Galerkin scheme-based solver. Numerical outcomes exhibit a strong concordance when contrasted with established experimental findings, providing a validation of the computational model. The computational findings showed that the flow properties of shock-driven elliptical gas inhomogeneity are significantly influenced by the Atwood number. This influence encompasses intricate wave patterns, alterations in bubble shape, vorticity generation, and features of the interface. When At > 0, the incoming shock wave outside the bubble and the transmitted shock wave inside the bubble diverge significantly. Complex wave patterns, including reflected and newly transmitted shock, are seen during the encounter. Interestingly, the transmitted shock and incident shock waves move with the same rates at At ≈ 0. While, compared to the incoming shock wave, the transmitted shock wave moves more quickly for At < 0. Subsequently, a detailed examination of the Atwood number effect is investigated by the creation of vorticity at the elliptical interface. Additionally, the study of vorticity generation processes was expanded to include significant spatial integrated fields such as kinetic energy, average vorticity, dilatational production, baroclinic production, and evolution of enstrophy. Finally, an extensive examination of the effects of the Atwood number on the flow dynamics was carried out through a quantitative analysis centered on the characteristics of the interface.

Conflict of Interest
The authors have no conflicts to disclose.

Acknowledgments
S.S. acknowledges funding through the German Research Foundation within the research unit DFG–FOR5409.

References

Brouillette, M. (2002). The Richtmyer-Meshkov instability. *Annual Review of Fluid Mechanics, 34*, 445-468. https://doi.org/10.1146/annurev.fluid.34.090101.162238.

Danaila, L., Voivenel, L., & Varea, E. (2017). Self-similarity criteria in anisotropic flows with viscosity stratification. *Physics of Fluids, 29*(2), 020716. https://doi.org/10.1063/1.4974520.

Daniel, L. (2020). Turbulence with large thermal and compositional density variations. *Annual Review of Fluid Mechanics*, *52*(1), 309-341. https://doi.org/10.1146/annurev-fluid-010719-060114.

Ding, J., Si, T., Chen, M., Zhai, Z., Lu, X., & Luo, X. (2017). On the interaction of a planar shock with a three-dimensional light gas cylinder. *Journal of Fluid Mechanics, 828*, 289-317. https://doi.org/10.1017/jfm.2017.528.

Haas, J.F., & Sturtevant, B. (1987). Interaction of weak shock waves with cylindrical and spherical gas inhomogeneities. *Journal of Fluid Mechanics, 181*, 41-76. https://doi.org/10.1017/s0022112087002003.

Haehn, N., Weber, C., Oakley, J., Anderson, M., Ranjan, D., & Bonazza, R. (2012). Experimental study of the shock–bubble interaction with reshock. *Shock Waves*, *22*, 47-56. https://doi.org/10.1007/s00193-011-0345-8.

Igra, D., & Igra, O. (2020). Shock wave interaction with a polygonal bubble containing two different gases, a numerical investigation. *Journal of Fluid Mechanics*, *889*, 1-20. https://doi.org/10.1017/jfm.2020.72.

Jacobs, J.W. (1992). Shock-induced mixing of a light-gas cylinder. *Journal of Fluid Mechanics, 234*, 629-649. https://doi.org/10.1017/s0022112092000946.

Jacobs, J.W. (1993). The dynamics of shock accelerated light and heavy gas cylinders. *Physics of Fluids, 5*(9), 2239-2247. https://doi.org/10.1063/1.858562.

Karchani, A. (2017). *Discontinuous Galerkin methods for the second-order Boltzmann-based hydrodynamic models*. (Ph.D. thesis) Department of Mechanical and Aerospace Engineering Graduate School, Gyeongsang National University, South Korea.

Krivodonova, L. (2007). Limiters for high-order discontinuous Galerkin methods. *Journal of Computational Physics, 226*(1), 879-896. https://doi.org/10.1016/j.jcp.2007.05.011.

Luo, X., Wang, M., Si, T., & Zhai, Z. (2015). On the interaction of a planar shock with an SF6 polygon. *Journal of Fluid Mechanics, 773*, 366-394. https://doi.org/10.1017/jfm.2015.257.

Meshkov, E.E. (1969). Instability of the interface of two gases accelerated by a shock wave. *Fluid Dynamics, 4*, 101-104. https://doi.org/10.1007/BF01015969.

Ranjan, D., Niederhaus, J.H.J., Oakley, J.G., Anderson, M.H., Bonazza, R., & Greenough, J.A. (2008). Shock-bubble interactions: Features of divergent shock-refraction geometry observed in experiments and simulations. *Physics of Fluids, 20*(3), 036101. https://doi.org/10.1063/1.2840198.

Ranjan, D., Oakley, J., & Bonazza, R. (2011). Shock-bubble interactions. *Annual Review of Fluid Mechanics, 43*, 117-140. https://doi.org/10.1146/annurev-fluid-122109-160744.

Richtmyer, R.D. (1960). Taylor instability in shock acceleration of compressible fluids. *Communications on Pure and Applied Mathematics, 13*, 297-319.

Si, T., Zhai, Z.G., Yang, J.M., & Luo, X.S. (2012). Experimental investigation of reshocked spherical gas interfaces. *Physics of Fluids, 24*(5), 054101. https://doi.org/10.1063/1.4711866.

Singh, S, Karchani, A., & Myong, R.S. (2018). Non-equilibrium effects of diatomic and polyatomic gases on the shock-vortex interaction based on the second-order constitutive model of the Boltzmann-Curtiss equation. *Physics of Fluids, 30*(1), 016109. https://doi.org/10.1063/1.5009122.

Singh, S. (2018). *Development of a 3D discontinuous Galerkin method for the second-order Boltzmann-Curtiss based hydrodynamic models of diatomic and polyatomic gases*. (Ph.D. thesis), Department of Mechanical and Aerospace Engineering Graduate School, Gyeongsang National University, South Korea.

Singh, S. (2020). Role of Atwood number on flow morphology of a planar shock-accelerated square bubble: A numerical study. *Physics of Fluids, 32*(12), 126112. https://doi.org/10.1063/5.0031698.

Singh, S. (2021a). Numerical investigation of thermal non-equilibrium effects of diatomic and polyatomic gases on the shock-accelerated light square bubble using a mixed-type modal discontinuous Galerkin method. *International Journal of Heat and Mass Transfer, 179*, 121708. https://doi.org/10.1016/j.ijheatmasstransfer.2021.121708.

Singh, S. (2021b). Contribution of Mach number to the evolution of Richtmyer-Meshkov instability induced by a shock-accelerated square light bubble. *Physical Review Fluids, 6*(10), 104001. https://doi.org/10.1103/PhysRevFluids.6.104001.

Singh, S. (2022). An explicit modal discontinuous Galerkin approach for compressible multicomponent flows: application to shock-bubble interaction. In: Uddin, Z., Awasthi, M.K., Asthana, R., Ram, M. (eds.) *Computing and Simulation for Engineers*, CRC, Boca Raton, pp. 18-36. https://doi.org/10.1201/9781003222255.

Singh, S. (2023). Investigation of aspect ratio effects on flow characteristics and vorticity generation in shock-induced rectangular bubble. *European Journal of Mechanics / B Fluids*, *101*, 131-148. https://doi.org/10.1016/j.euromechflu.2023.05.006.

Singh, S., & Battiato, M. (2021a) An explicit modal discontinuous Galerkin method for Boltzmann transport equation under electronic nonequilibrium conditions. *Computers and Fluids, 224*, 104972. https://doi.org/10.1016/j.compfluid.2021.104972.

Singh, S., & Battiato, M. (2021b). Behavior of a shock-accelerated heavy cylindrical bubble under non-equilibrium conditions of diatomic and polyatomic gases. *Physical Review Fluids, 6*(4), 044001. https://doi.org/10.1103/PhysRevFluids.6.044001.

Singh, S., & Battiato, M. (2022). Numerical simulations of Richtmyer-Meshkov instability of SF6 square bubble in diatomic and polyatomic gases. *Computers & Fluids, 242*, 105502. https://doi.org/10.1016/j.compfluid.2022.105502.

Singh, S., & Battiato, M. (2023). Investigation of shock Mach number effects on the growth of convergent Richtmyer-Meshkov instability in a heavy square bubble. *Physica D: Nonlinear Phenomena, 453*, 133844. https://doi.org/10.1016/j.physd.2023.133844.

Singh, S., & Jalleli, D.T. (2023). Investigation of coupling effect on the evolution of Richtmyer–Meshkov instability at double heavy square bubbles. *Science China Physics, Mechanics & Astronomy*, *67*(1), 214711. https://doi.org/10.1007/s11433-023-2218-2.

Singh, S., & Msmali, A.H. (2023) On the spatiotemporal pattern formation in nonlinear coupled reaction–diffusion systems. *Axioms, 12*(11), 1004. https://doi.org/10.3390/axioms12111004.

Singh, S., & Torrilhon, M. (2023). On the shock-driven hydrodynamic instability in square and rectangular light gas bubbles: a comparative study from numerical simulations. *Physics of Fluids, 35*(1), 012117. https://doi.org/10.1063/5.0137543.

Singh, S., Battiato, M., & Myong, R.S. (2021a). Impact of bulk viscosity on flow morphology of shock-accelerated cylindrical light bubble in diatomic and polyatomic gases. *Physics of Fluids, 33*(6), 066103.

Singh, S., Battiato, M., & Myong, R.S. (2021b). Impact of the bulk viscosity on flow morphology of shock-bubble interaction in diatomic and polyatomic gases. *Physics of Fluids, 33*(6), 066103. https://doi.org/10.1063/5.0051169.

Singh, S., Karchani, A., Chourushi, T., & Myong, R.S. (2022). A three-dimensional modal discontinuous Galerkin method for the second-order Boltzmann-Curtiss-based constitutive model of rarefied and microscale gas flows. *Journal of Computational Physics, 457*, 111052. https://doi.org/10.1016/j.jcp.2022.111052.

Singh, S., Mittal, R.C., Thottoli, S.R., Tamsir, M. (2023) High-fidelity simulations for Turing pattern formation in multi-dimensional Gray–Scott reaction-diffusion system. *Applied Mathematics and Computation, 452*, 128079. https://doi.org/10.1016/j.amc.2023.128079.

Zeng, W.G., Pan, J.H., Sun, Y.T., & Ren, Y.X. (2018). Turbulent mixing and energy transfer of reshocked heavy gas curtain. *Physics of Fluids, 30*(6), 064106. https://doi.org/10.1063/1.5032275.

Zhai, Z., Wang, M., Si, T. & Luo, X. (2014). On the interaction of a planar shock with a light polygonal interface. *Journal of Fluid Mechanics, 757*, 800-816. https://doi.org/10.1017/jfm.2014.516.

Zhai, Z.G., Si, T., Luo, X.S., & Yang, J.M. (2011). On the evolution of spherical gas interfaces accelerated by a planar shock wave. *Physics of Fluids, 23*(8), 084104. https://doi.org/10.1063/1.3623272.

Zhou, Y. (2017a). Rayleigh-Taylor and Richtmyer-Meshkov instability induced flow, turbulence, and mixing. I. *Physics Reports, 720-722*, 1-136. https://doi.org/10.1016/j.physrep.2017.07.005.

Zhou, Y. (2017b). Rayleigh-Taylor and Richtmyer-Meshkov instability induced flow, turbulence, and mixing. II. *Physics Reports, 723-725*, 1-160. https://doi.org/10.1016/j.physrep.2017.07.008.

Zhou, Y., Williams, R.J., Ramaprabhu, P., Groom, M., Thornber, B., Hillier, A., Mostert, W., Rollin, B., Balachandar, S., Powell, P.D., Mahalov, A., & Attal, N. (2021). Rayleigh-Taylor and Richtmyer-Meshkov instabilities: A journey through scales. *Physica D: Nonlinear Phenomena, 423*, 132838. https://doi.org/10.1016/j.physd.2020.132838.

Zhu, Y., Yang, Z., Luo, K.H., Pan. J., & Pan, Z. (2019). Numerical investigation of planar shock wave impinging on spherical gas bubble with different densities. *Physics of Fluids, 31*(5), 056101. https://doi.org/10.1063/1.5092317.